FeNi3-FeNi3N-a high-performance catalyst for overall water splitting

$FeNi_3$-$FeNi_3N$ – a High-performance Catalyst for Overall Water Splitting

Shuqin Liang,[1,2†] Meizan Jing,[2†] Tiju Thomas,[3] Jian Liu,[2] Haichuan Guo,[1] J. Paul Attfield,[4] Ali Saad,[1] Hangjia Shen,[*1] Minghui Yang[*1]

1.Solid State functional Materials Research Laboratory, Ningbo Institute of Materials Technology and Engineering, Chinese Academy of Sciences, Ningbo 315201, China.

2.State Key Laboratory of Heavy Oil Processing and Beijing Key Lab of Oil & Gas Pollution Control, China University of Petroleum, Beijing 102249, China.

3.Department of Metallurgical and Materials Engineering, and DST Solar Energy Harnessing Center , Indian Institute of Technology Madras, Adyar, Chennai 600036, Tamil Nadu, India.

4.Centre for Science at Extreme Conditions and School of Chemistry University of Edinburgh ,King's Buildings, Mayfield Road, Edinburgh, EH9 3JZ, United Kingdom.

† These authors contributed equally to this work.

Abstract:

The design and development of non-precious metal catalysts with high activity and stability for overall water splitting remains a major challenge. Herein, lamellar $FeNi_3N$ incorporated by $FeNi_3$ is synthesized via thermal ammonolysis. The abundance of hollow sites in this $FeNi_3$-$FeNi_3N$ heterostructure significantly enhances the intrinsic activity towards hydrogen evolution reaction, while the heterostructure also offers high electrochemical active surface area for oxygen evolution reaction. $FeNi_3$-$FeNi_3N$ enables a lower overpotential for both hydrogen and oxygen evolution

electrocatalysis in alkaline media. When $FeNi_3$-$FeNi_3N$ is employed as a bifunctional material for overall water splitting, it shows a cell voltage of only 1.5 V at 10 mA cm^{-2} and offers stable performance for up to 48 h at current densities of ~40 mA cm^{-2}.

Introduction

Electrochemical water splitting is a promising, sustainable technology to enable energy conversion and high purity hydrogen production. This is so significant since it can be a means to achieve comprehensive utilization of renewable resource-derived electricity.[1] The efficiency of electrochemical water splitting depends primarily on electrode catalysts for both anodic oxygen evolution reaction (OER) and cathodic hydrogen evolution reaction (HER).[2-4] In typical acidic media, the electrode materials deployed until now are generally noble metal-based materials, which suffer from high overpotential, cost and vulnerability.[5] On the contrary, although the output power of overall water splitting in alkaline medium is two orders of magnitude lower than that in acidic solution,[6-7] the low overpotentials achieved on earth-abundant transition metal materials make overall alkaline water splitting more efficient and economical.

Nickel/iron based compounds (including alloys,[11] layer double hydroxide,[12] nitrides,[13] oxides,[14] sulfides,[15] phosphides,[16] carbides[17-18]) have been known to be active OER catalysts. Among these materials, the as-formed NiOOH site is commonly regarded as the active center, and the incorporation of Fe suppresses the oxidation of Ni^{2+}; leading to $Ni^{3+}/^{4+}$ with more oxidizing power and thus resulting in faster OER

kinetics.[12, 19-21] It is reported that the number of Ni^{2+} ions that get converted into Ni^{3+} ions (NiOOH) is equal to the number of Ni sites that actually catalyze the OER;[22] this allows the accurate determination of density of active sites via a redox peak method.[22] To futher simplify the electrochemical system and speed up the commercialization of alkaline water splitting, the efficient bifunctional electrocatalysts that simultaneously catalyze HER and OER in alkaline media is desirable.[8-10] However, due to the inappropriate (either too strong or too weak) binding energy toward H^+,[23-24] the NiFe based materials still suffer from inferior HER activity;[25] hence the preparation of possible bifunctional NiFe-based catalysts for efficient OER and HER remains a challenge.

Here, we describe a lamellar $FeNi_3$-$FeNi_3N$ catalyst prepared using a facile hydrothermal method, followed by nitridation. The $FeNi_3N$ nanospheres are in situ formed and dispersed rather well on the surface of lamella like $FeNi_3$ matrix during thermal nitridation. This gives rise to the formation of $FeNi_3$-$FeNi_3N$ heterostructures at the interface of $FeNi_3N$ and $FeNi_3$. Density functional theory (DFT) calculations indicate that some hollow sites that exist in $FeNi_3$-$FeNi_3N$ heterostructures show a lower Gibbs free energy for adsorbed atomic hydrogen, and therefore it contributes to high activity toward HER. Simultaneously, the $FeNi_3N$ nanospheres enhance the number of accessible electrochemical active sites for OER, and hence dramatically increase the specific activity toward OER. For demonstrating practical use of $FeNi_3$-$FeNi_3N$ catalysts - both HER and OER are run in alkaline media within a symmetric alkaline water electrolyzer. The electrolyzer is assembled using efficient

$FeNi_3$-$FeNi_3N$ as anodic and cathodic materials; the device displays a low overpotential with 1.5 V cell voltage at 10 mA cm^{-2} current density.

Results and discussion

The lamella like $FeNi_3$-$FeNi_3N$ is synthesized through a facile two-step strategy. As shown in **Figure** 1a; ferric nitrate and the nickel nitrate are first dissolved into the mixture of cis-9-octadecenylamine and butyl alcohol solvents to form a homogeneous solution. The collected NiFe hydroxide through hydrothermal treatment is then heat treated under ammonia flow to achieve nitridation.

The X-ray diffraction (XRD) pattern of the $FeNi_3$ in **Figure** S1 matches well with that of $FeNi_3$ alloy (PDF#38-0419). In addition to the $FeNi_3$ alloy phase, cubic $FeNi_3N$ (PDF#50-1434)[15, 25] featured peaks at 41.52°, 48.34° and 70.81° are observed for the $FeNi_3N$-$FeNi_3$ sample annealed in ammonia at 460 °C (**Figure** 1b). The Rietveld refined result suggests the ratio of cubic $FeNi_3N$ and $FeNi_3$ crystalline phase is 22:78. The XRD patterns of samples calcined at different temperatures are shown in **Figure** S2, and it clearly shows that $FeNi_3$ alloy would be gradually converted into $FeNi_3N$ with the increase of temperature. When the nitriding temperature is increased to 650 °C, only pure phase of $FeNi_3N$ is formed in **Figure** S1. The crystal structure is further confirmed by transmission electron microscopy (TEM). For $FeNi_3$ in **Figure** S3b, the lattice fringes with d-spacing of 0.18 and 0.20 nm correspond to the (200) and (111) plane of cubic $FeNi_3$. After nitridation at a relatively high temperature of 650 °C for 2 h, the observed lattice fringes in the sample show a d-spacing of 0.22 nm, which is attributed to the (111) plane of cubic $FeNi_3N$ (**Figure** S3d). Correspondingly,

both $FeNi_3$ and $FeNi_3N$ featured lattice fringes are clearly observed in TEM images for $FeNi_3$-$FeNi_3N$ (**Figure** 1d). Their nano domains are adjacent with a discernible interface, clearly showing the formation of $FeNi_3$-$FeNi_3N$ heterostructure.[26-28] Investigated by scanning electron microscopy (SEM) in **Figure** 1e and **Figure** S4, similar to pristine $FeNi_3$ alloy, $FeNi_3$-$FeNi_3N$ maintains a lamella like morphology. However, the aggregation driven by high temperature leads to the transformation of morphology to sphere for $FeNi_3N$.

Electrocatalytic activity of as-prepared catalysts for HER is evaluated in 1.0 M KOH using a typical three-electrode system. A high purity of graphite rod is used as the counter electrode. Commonly, the overpotential at current density of 10 mA cm^{-2} (η_{10}) is taken as the reference for HER activity assessment. As shown in **Figure 2**a, the HER overpotential of $FeNi_3$-$FeNi_3N$ (51 mV) is closed to the value for Pt/C (40 mV), which in turn is far better than that in case of $FeNi_3N$ and $FeNi_3$ nanocatalysts. And the overpotential (η) observed at 20 and 100 mA cm^{-2} is 86 mV and 215 mV respectively, which slightly higher than Pt/C (55 mV and 156 mV based on current densities). In the **Figure** S5, it can be seen that the performance of $FeNi_3$-$FeNi_3N$ for HER decrease with increasing temperature, and the sample calcined at 460 °C is the best. Specifically, the HER overpotential (η) of $FeNi_3$-$FeNi_3N$ outperforms many FeNi-based materials in **Table** S1. Correspondingly, the Tafel slope in **Figure** 2b of $FeNi_3$-$FeNi_3N$ is 83 mV $decade^{-1}$, which suggests the Volmer- Heyrovsky mechanism as the HER pathway, in which the Heyrovsky process ($H_2O+H_{ads}+e^- \rightarrow H_2+OH^-$) is the rate-determining step (RDS). Inversely, the higher Tafel slope of $FeNi_3$ (182 mV dec^{-1})

and $FeNi_3N$ (264 mV dec^{-1}) indicates that the Volmer reaction dominates the HER kinetics.

Electrochemical impedance spectroscopy (EIS) analysis is performed on at η =70 mV. As depicted in **Figure** S6 and **Table** S2, the semicircle of $FeNi_3$-$FeNi_3N$ in Nyquist plots indicates a charge transfer resistance (R_{ct}) of 55.2 Ω, which is smaller than that of $FeNi_3$ (67.4 Ω) and $FeNi_3N$ (238.4 Ω). The low R_{ct} reveals that $FeNi_3$-$FeNi_3N$ exhibits fast charge transfer rates, consistent with the HER activity. As shown in **Figure** S7, the double-layer capacitance (C_{dl}) is tested by the cyclic voltammetry method at different scan rate. Based on this, the corresponding calculated result listed in **Table** S2 suggests $FeNi_3$-$FeNi_3N$ possesses the largest electrochemical active surface area (ECSA) of 7.1 m^2 g^{-1}_{cat}.

To assess the kinetic barriers involved in HER, we have studied the effect of temperature on the performance of the catalysts (**Figure** 2d and **Figure** S8). HER proceeds more rapidly at elevated temperatures, reflecting the exponential temperature dependence of the chemical rate constant. The Arrhenius plots at η = 100 mV for three different catalysts allow extraction of electrochemical activation energies (E_a). As shown in **Figure** 2d, $FeNi_3$-$FeNi_3N$ exhibit an E_a of 55.9 kJ mol^{-1}, which is lower than that in case of $FeNi_3$ (83.1 kJ mol^{-1}) or $FeNi_3N$ (154.3 kJ mol^{-1}). This result suggests the lowest apparent barrier for HER on $FeNi_3$-$FeNi_3N$ heterostructures.

To better understand the reason for catalytic activity of $FeNi_3N$, $FeNi_3$ and $FeNi_3$-$FeNi_3N$ heterostructure toward HER, density functional theory (DFT)

calculations are used for constructing the correlative theoretical models (**Figure** S15-18) and for calculating the free energy of H* (ΔG(H*)) on them (**Table** S3-S5). Generally, a site with moderate value of |ΔG(H*)|≈0 is most active for the HER.[29-30] The most active sites for $FeNi_3N$, $FeNi_3$ and $FeNi_3$-$FeNi_3N$ are portrayed in **Figure** 2c. As shown in **Figure** 2e, the corresponding Gibbs free energy diagram of HER reveal that the hollow sites H2 (Fe-Ni-Ni) and H3 (Ni-Ni-Ni) in $FeNi_3$-$FeNi_3N$ possess the lowest |ΔG(H*)| value of 0.01 and 0.07 eV, confirming relatively more favorable H* adsorption kinetics on $FeNi_3$-$FeNi_3N$ heterostructures during the HER process. In order to identify the effect of $FeNi_3$-$FeNi_3N$ interface on electronic structure, charge density difference is calculated (**Figure S**19). Yellow and blue areas represent charge density increase and reduction, respectively. The electrons transferred from $FeNi_3N$ to $FeNi_3$ leads to make the yellow areas are more close to $FeNi_3$. The abundant charge accumulation on $FeNi_3$ leads to a higher catalytic activity for $FeNi_3$-$FeNi_3N$ interface than pristine $FeNi_3N$ or $FeNi_3$. The stability of the HER catalysts is investigated using chronoamperometric measurement at a current density of 10 mA cm^{-2}, continuously for 11 hours. As presented in **Figure** S9, $FeNi_3$-$FeNi_3N$ shows an initial overpotential of 40 mV, which is same as that of the Pt/C electrode. And no appreciable increase in overpotential is observed in this time interval. While for Pt/C, there is an increase of 117 mV observed.

The OER polarization curves **(Figure** 3a) collected via negative scan in 1.0 M KOH, shows an apparent peak at 1.30-1.40 V for Ni containing samples. This peak could be assigned to reduction of Ni^{3+} to Ni^{2+}. And the OER current appears earliest

at 1.44 V for $FeNi_3$-$FeNi_3N$. At the OER current density of 10 mA cm^{-2}, an overpotential of 260 mV is needed for $FeNi_3$-$FeNi_3N$. By comparison, it is 280 mV, 270 mV and 370 mV for $FeNi_3$, $FeNi_3N$ and IrO_2, respectively. And in terms of the polarization curves in **Figure** S10, we can find the material calcined at 460°C is the most favorable for OER. The $FeNi_3$-$FeNi_3N$ with heterostructure exhibit the smallest Tafel slope of 53 mV dec^{-1} (**Figure** S11), clearly indicating faster reaction kinetics in this case.

It is commonly known that the NiOOH which is in-situ formed during OER offers active sites in case of NiFe-based materials.[12, 19] Thus, in terms of the reduction peak of Ni^{3+}/Ni^{2+}, the accessible active sites of Ni can be quantified using turnover frequency (TOF) calculation.[19, 22, 31] As shown in **Figure** 3b, the reduction peak at range from 1.3 to 1.4 V is assigned to Ni^{3+}/Ni^{2+}.[16] Compared to $FeNi_3$ (0.185 mW cm^{-2}) and $FeNi_3N$ (0.368 mW cm^{-2}), the largest peak area of 0.618 mW cm^{-2} for $FeNi_3$-$FeNi_3N$ indicates that the $FeNi_3$-$FeNi_3N$ heterostructure improves the density of accessible Ni site. Furthermore, the highest TOF is achieved on $FeNi_3$-$FeNi_3N$, which indicates superior OER intrinsic activity of $FeNi_3$-$FeNi_3N$ catalyst. As shown in **Figure** 3c and **Table** S6, at overpotential of 300 mV, the TOF of $FeNi_3$-$FeNi_3N$ is 0.32 s^{-1}, which exceeds that of $FeNi_3$(0.20 s^{-1}) and $FeNi_3N$ (0.14 s^{-1}). In addition, as shown in **Figure** S12, a much lower R_{ct} on $FeNi_3$-$FeNi_3N$ (7.0 Ω cm^2) than that of $FeNi_3$ (16.6 Ω cm^2) and $FeNi_3N$ (18.8 Ω cm^2) also indicates faster interfacial electron transfer kinetics between $FeNi_3$-$FeNi_3N$ and electrolyte during oxygen evolution.

The OER durability for the prepared materials is evaluated via galvanostatic method at 10 mA cm^{-2}. As shown in **Figure** S13, the OER catalyzed on $FeNi_3$-$FeNi_3N$ exhibits a lowest initial potential of 260 mV. And during a 11 h test, the potential remained unchanged; this reveals a substantial durability of $FeNi_3$-$FeNi_3N$ for OER.

As shown in **Figure** S14, our $FeNi_3$-$FeNi_3N$ catalyst needs much lower overpotential at a current density of 10 mA cm^{-2} for both HER (40 mV) and OER (260 mV) in 1.0 M KOH. This is clearly desirable performance in comparison to other reported transition metal-based electrocatalysts. Considering that the $FeNi_3$-$FeNi_3N$ has exceptional HER and OER properties, we employed $FeNi_3$-$FeNi_3N$ modified nickel foam (NF) as the cathode and anode to fabricate a symmetric electrolyzer for overall water splitting.

Figure 4a depicts the polarization curve of water splitting. The $FeNi_3$-$FeNi_3N$/NF exhibits excellent performance: only a 1.5 V cell voltage is needed to deliver a 10 mA cm^{-2} current density; this is much lower than most of reported values (**Figure** 4b and **Table** S7). The lower of cell voltage; the more efficient and less expensive would the water splitting be. For different current densities, the corresponding voltage is found to be consistent with the potential difference (ΔV) between HER and OER measured in a three-electrode system for $FeNi_3$-$FeNi_3N$ (**Figure** 4c).

The electrolyzer demonstrates good long-term catalytic durability, sustaining constant galvanostatic electrolysis for up to 48 h at a controllable current density (10 to 40 mA cm^{-2}) with negligible degradation (**Figure 4**d). This suggests excellent

potential for practical applications. The Faradaic efficiency (FE) of $FeNi_3$-$FeNi_3N$ for the HER and OER is measured quantitatively from the total amount of charge passed through the cell during electrolysis and the total amount of evolved gas collected by water–gas displacement method.[32] The amount of generated H_2 and O_2 matches well with the theoretically calculated amount under total charge during the electrolysis process (**Figure** 4e). This suggests that the FE is close to 100% for both HER and OER, with the ratio of H_2 and O_2 being close to 2:1.

Conclusions

We report that $FeNi_3$-$FeNi_3N$ heterostructure offers excellent bifunctional catalytic performance towards HER and OER. This is due to the formation of highly active Fe-Ni-Ni and Ni-Ni-Ni hollow sites for HER and a large amount of electrochemically active sites available for OER on the $FeNi_3$-$FeNi_3N$ heterostructure. The excellent HER and OER activities makes this catalyst suitable for both electrodes, and renders it directly relevant for overall water splitting. A demonstration electrolyzer exhibits a low driving voltage of 1.50 V at the current density of 10 mA cm^{-2}. Furthermore, the heterostructureelectrocatalyst exhibits remarkable activity with a negligible decay after 48h of operation.

Conflicts of interest

There are no conflicts to declare.

Acknowledgements

This work is supported by Natural Science Foundation of China (Grant No. 21471147) and National Key Research and Development Plan (Grant No. 2016YFB0101205). HS would like to thank the China Postdoctoral Science Foundation (2019M652155). MY would like to thank the National "Thousand Youth Talents" program of China and Ningbo 3315 program for support. Tiju Thomas thanks DSEHC, Ministry of Electronics and Information Technology (Project ID: ELE1819353MEITNAK), and DST (Project ID: MET1617146DSTXTIJU, YSS/2015/001712 and DST/TMD/SERI/HUB/1(C)) for supporting this research work.

References

1. Popczun, E. J.; McKone, J. R.; Read, C. G.; Biacchi, A. J.; Wiltrout, A. M.; Lewis, N. S.; Schaak, R. E., *J Am Chem Soc* **2013,** 135 (25), 9267-70.
2. Zhu, C.; Wang, A. L.; Xiao, W.; Chao, D.; Zhang, X.; Tiep, N. H.; Chen, S.; Kang, J.; Wang, X.; Ding, J.; Wang, J.; Zhang, H.; Fan, H. J., *Adv Mater* **2018,** 30 (13), e1705516.
3. Zhang, G.; Feng, Y.-S.; Lu, W.-T.; He, D.; Wang, C.-Y.; Li, Y.-K.; Wang, X.-Y.; Cao, F.-F., *ACS Catalysis* **2018,** 8 (6), 5431-5441.
4. Liang, S.; Jing, M.; Pervaiz, E.; Guo, H.; Thomas, T.; Song, W.; Xu, J.; Saad, A.; Wang, J.; Shen, H.; Liu, J.; Yang, M., *ACS applied materials & interfaces* **2020,** 12 (37), 41464-41470.
5. Yan, X.; Tian, L.; Li, K.; Atkins, S.; Zhao, H.; Murowchick, J.; Liu, L.; Chen, X., *Advanced Materials Interfaces* **2016,** 3 (22), 1600368.
6. Chen, Z.; Song, Y.; Cai, J.; Zheng, X.; Han, D.; Wu, Y.; Zang, Y.; Niu, S.; Liu, Y.; Zhu, J.; Liu, X.; Wang, G., *Angew Chem Int Ed Engl* **2018,** 57 (18), 5076-5080.
7. McCrory, C. C.; Jung, S.; Peters, J. C.; Jaramillo, T. F., *J Am Chem Soc* **2013,** 135 (45), 16977-87.
8. Zeng, K.; Zhang, D., *Progress in Energy and Combustion Science* **2010,** 36 (3), 307-326.

9. Danilovic, N.; Subbaraman, R.; Strmcnik, D.; Chang, K. C.; Paulikas, A. P.; Stamenkovic, V. R.; Markovic, N. M., *Angew Chem Int Ed Engl* **2012,** 51 (50), 12495-8.
10. Gong, M.; Dai, H., *Nano Research* **2014,** 8 (1), 23-39.
11. Zheng, F.; Zhang, Z.; Xiang, D.; Li, P.; Du, C.; Zhuang, Z.; Li, X.; Chen, W., *J Colloid Interface Sci* **2019,** 555, 541-547.
12. Yin, S.; Tu, W.; Sheng, Y.; Du, Y.; Kraft, M.; Borgna, A.; Xu, R., *Adv Mater* **2018,** 30 (5), 1705106.
13. Xie, J.; Carrasco, J.; Li, R.; Shen, H.; Chen, Q.; Yang, M., *Journal of Power Sources* **2019,** 431, 226-231.
14. Dong, C.; Kou, T.; Gao, H.; Peng, Z.; Zhang, Z., *Advanced Energy Materials* **2018,** 8 (5), 1701347.
15. Cheng, N.; Liu, Q.; Asiri, A. M.; Xing, W.; Sun, X., *Journal of Materials Chemistry A* **2015,** 3 (46), 23207-23212.
16. Zhang, R.; Wang, X.; Yu, S.; Wen, T.; Zhu, X.; Yang, F.; Sun, X.; Wang, X.; Hu, W., *Adv Mater* **2017,** 29 (9), 1605502.
17. Zhou, Z.; Yuan, Z.; Li, S.; Li, H.; Chen, J.; Wang, Y.; Huang, Q.; Wang, C.; Karahan, H. E.; Henkelman, G.; Liao, X.; Wei, L.; Chen, Y., *Small* **2019,** 15 (11).
18. Lu, X. F.; Yu, L.; Zhang, J.; Lou, X. W., *Adv. Mater.* **2019,** 31 (30), 1900699.
19. Gorlin, M.; Chernev, P.; Ferreira de Araujo, J.; Reier, T.; Dresp, S.; Paul, B.; Krahnert, R.; Dau, H.; Strasser, P., *J Am Chem Soc* **2016,** 138 (17), 5603-14.
20. Yanjie, W.; Nana, Z.; Baizeng, F.; Hui, L.; Xiaotao, B. T.; Haijiang, W., *Chem. Rev.* **2015,** 115 (9), 3433-67.
21. Friebel, D.; Louie, M. W.; Bajdich, M.; Sanwald, K. E.; Cai, Y.; Wise, A. M.; Cheng, M. J.; Sokaras, D.; Weng, T. C.; Alonso-Mori, R.; Davis, R. C.; Bargar, J. R.; Norskov, J. K.; Nilsson, A.; Bell, A. T., *J Am Chem Soc* **2015,** 137 (3), 1305-13.
22. Anantharaj, S.; Kundu, S., *ACS Energy Letters* **2019,** 4 (6), 1260-1264.
23. Zhu, J.; Hu, L.; Zhao, P.; Lee, L. Y. S.; Wong, K.-Y., *Chem. Rev.* **2020,** 120 (2), 851-918.
24. Suryanto, B. H. R.; Wang, Y.; Hocking, R. K.; Adamson, W.; Zhao, C., *Nat Commun* **2019,** 10 (1), 5599.
25. Liu, X.; Lv, X.; Wang, P.; Zhang, Q.; Huang, B.; Wang, Z.; Liu, Y.; Zheng, Z.; Dai, Y., *Electrochim. Acta* **2020,** 333.
26. Ye, C.; Jiao, Y.; Jin, H.; Slattery, A. D.; Davey, K.; Wang, H.; Qiao, S. Z., *Angew Chem Int Ed Engl* **2018,** 57 (51), 16703-16707.
27. Yang, F.; Bao, X.; Li, P.; Wang, X.; Cheng, G.; Chen, S.; Luo, W., *Angew Chem Int Ed Engl* **2019,** 58 (40), 14179-14183.
28. Zhang, G.; Chen, D.; Li, N.; Xu, Q.; Li, H.; He, J.; Lu, J., *Angew Chem Int Ed Engl* **2020,** 59 (21), 8255-8261.
29. Kresse, G.; Furthmüller, J., *Computational materials science* **1996,** 6 (1), 15-50.
30. Blöchl, P. E., *Physical review B* **1994,** 50 (24), 17953.

31. Zhang, R.; Zhang, Y.-C.; Pan, L.; Shen, G.-Q.; Mahmood, N.; Ma, Y.-H.; Shi, Y.; Jia, W.; Wang, L.; Zhang, X.; Xu, W.; Zou, J.-J., *ACS Catalysis* **2018,** 8 (5), 3803-3811.
32. Pu, Z.; Amiinu, I. S.; Kou, Z.; Li, W.; Mu, S., *Angewandte Chemie-International Edition* **2017,** 56 (38), 11559-11564.

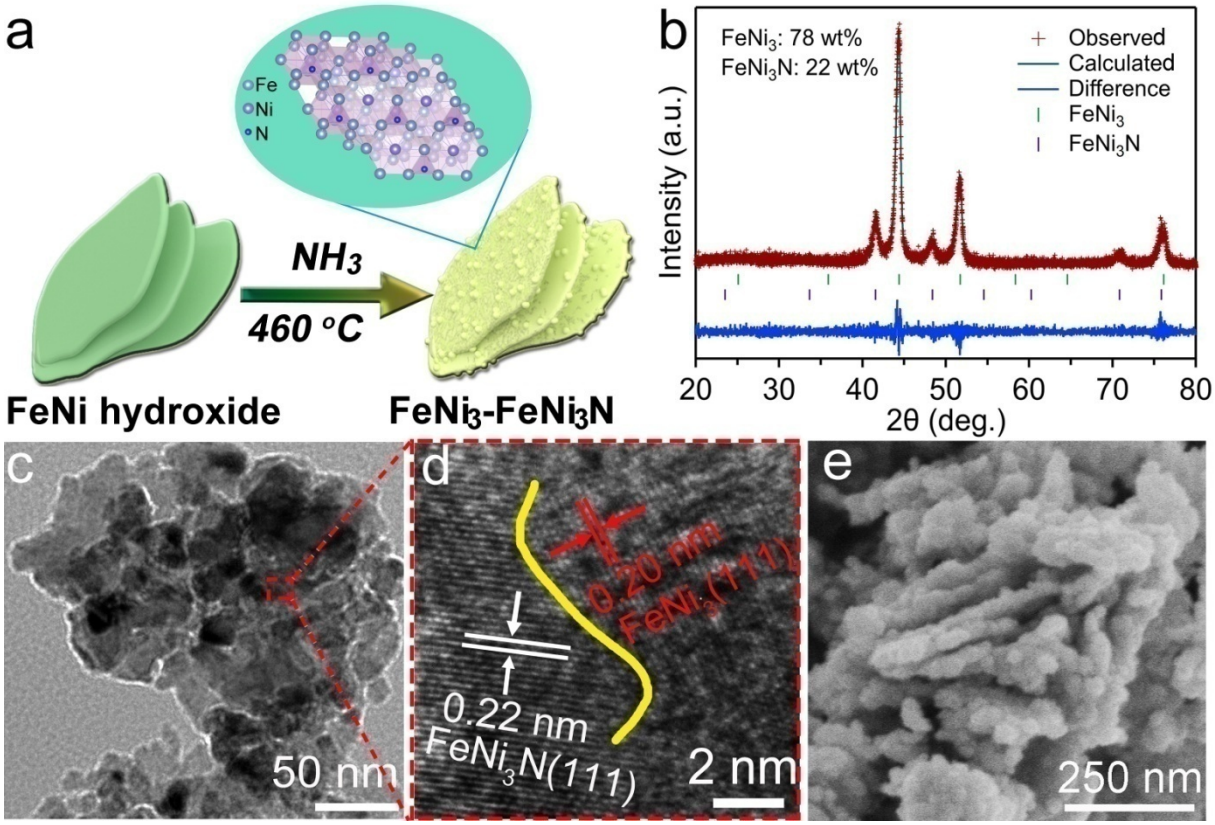

Figure 1.(a) Schematic diagram of the synthesis of $FeNi_3$-$FeNi_3N$ samples. (b) The Rietveld refined XRD pattern of $FeNi_3$-$FeNi_3N$. (c-d) Show the TEM and the HR-TEM of $FeNi_3$-$FeNi_3N$. (e) The SEM of $FeNi_3$-$FeNi_3N$.

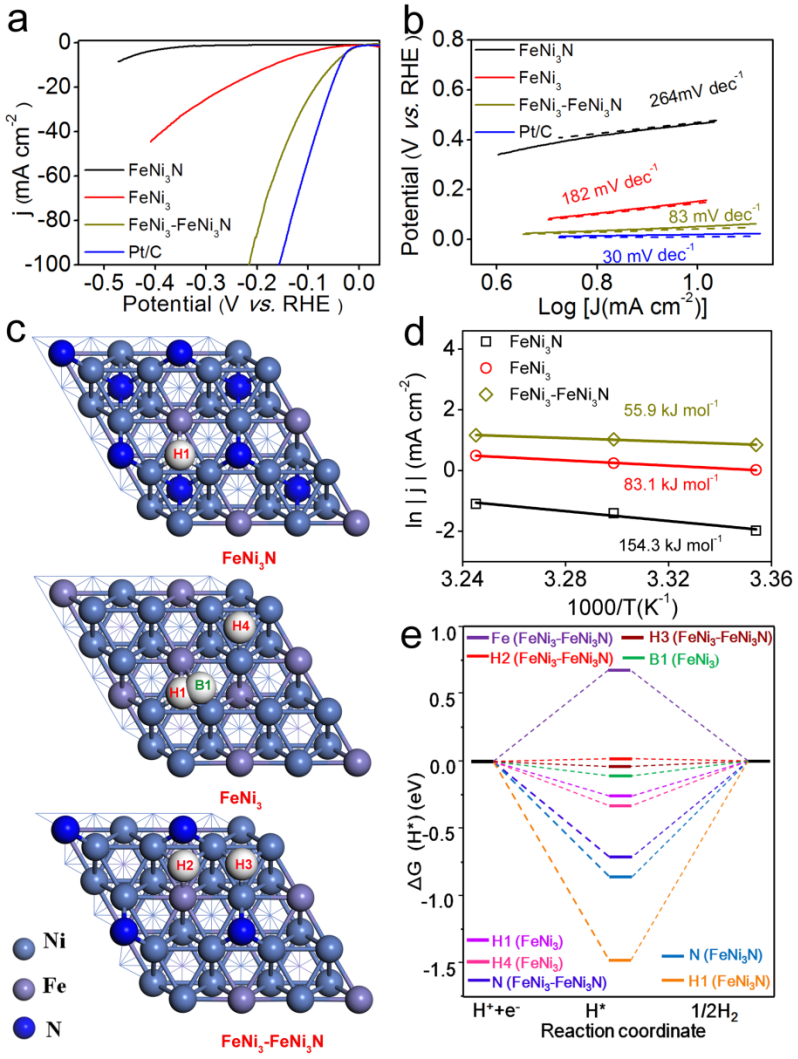

Figure 2.(a) LSV curves of $FeNi_3$-$FeNi_3N$ with different calcination temperatures, $FeNi_3N$, $FeNi_3$, and Pt/C for HER in 1.0 M KOH. (b) Tafel plots for the samples towards HER. (c) Optimized structures of $FeNi_3N(111)$, $FeNi_3(111)$, $FeNi_3$-$FeNi_3N$ heterostructure and possible adsorption sites of H* on them. (d) The HER Arrhenius plot of the inverse temperature versus the Ln. of the exchange current density for $FeNi_3$, $FeNi_3N$ and $FeNi_3$-$FeNi_3N$. (e) Calculated free-energy diagram of HER over $FeNi_3N(111)$, $FeNi_3(111)$ and $FeNi_3$-$FeNi_3N$ heterostructure at equilibrium potential.

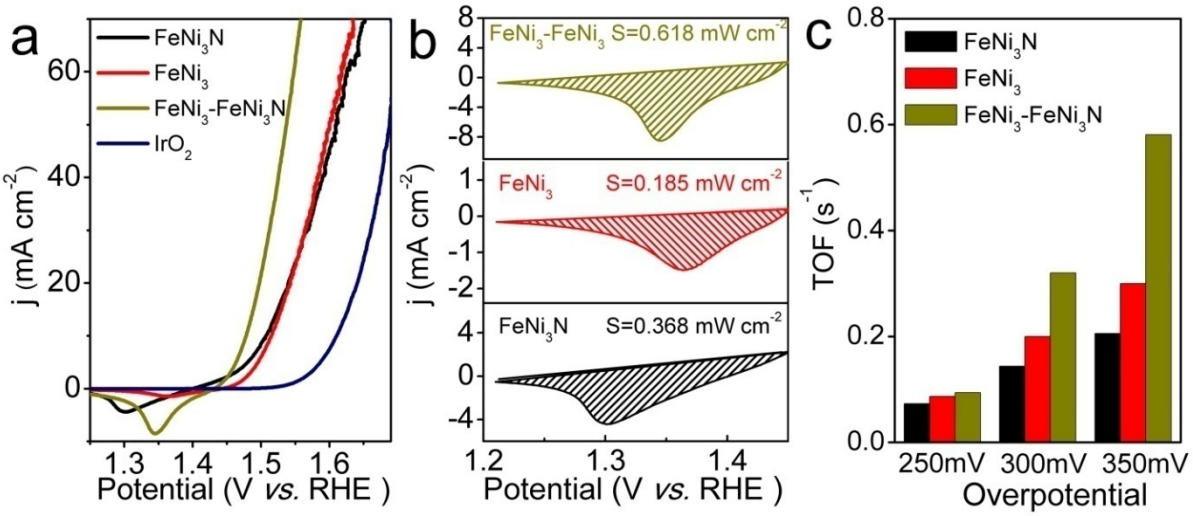

Figure 3.(a) LSV curves of $FeNi_3$-$FeNi_3N$ with different calcination temperatures, $FeNi_3N$, $FeNi_3$, and IrO_2 for OER in 1.0 M KOH. (b) The calculated area of the reduction peak of nickel during OER in KOH. (c) TOF of different catalysts at various applied potentials.

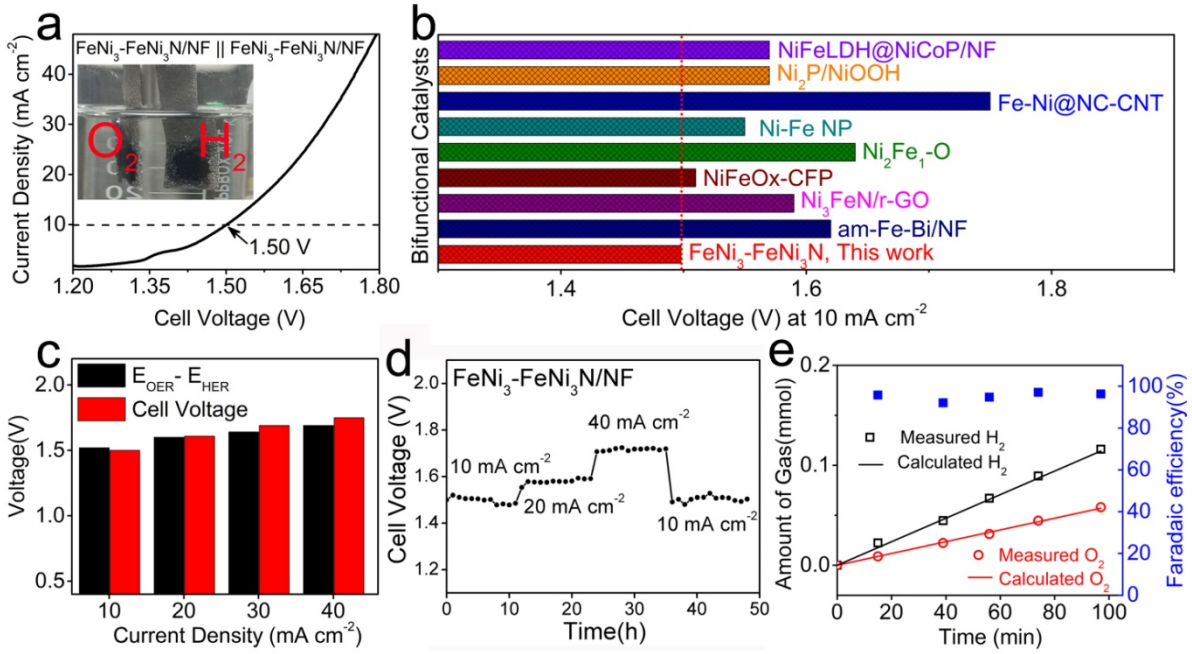

Figure 4.(a) Polarization curves of $FeNi_3$-$FeNi_3N$/NF || $FeNi_3$-$FeNi_3N$/NF water electrolyzer in 1.0 M KOH. The inset shows H_2 and O_2 bubbles evolving from $FeNi_3$-$FeNi_3N$/NF electrodes. (b) Comparison of the water splitting performance of $FeNi_3$-$FeNi_3N$/NF with other recent reported bifunctionalelectrocatalysts. (c) Cell voltage in a two-electrode configuration and the polarization curves of the voltage difference (ΔV) between HER and OER in a three-electrode system for $FeNi_3$-$FeNi_3N$. (d) Time-dependent current density curve for $FeNi_3$-$FeNi_3N$ in a two-electrode configuration at a current of 10, 20, 40 mA cm^{-2}.use smaller scale e.g. 1-2 V (e) Amount of gas collected and calculated from electric quantity for $FeNi_3$-$FeNi_3N$ during overall water splitting, and the Faraday efficiency (FE), as calculated from hydrogen collected